F. Symalla, S. Heidrich, P. Friederich,
T. Strunk, T. Neumann, D. Minami,
D. Jeong, W. Wenzel* 1900222

**Multiscale Simulation of
Photoluminescence Quenching in
Phosphorescent OLED Materials**
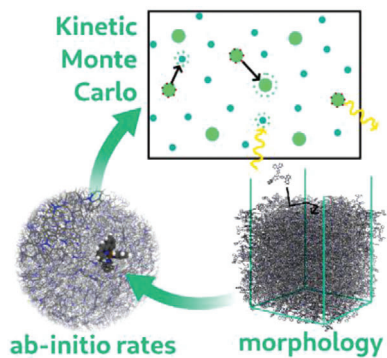
A multiscale simulation protocol to treat triplet–triplet annihilation (TTA) in phosphorescent organic light-emitting diodes (PhOLEDs), in which microscopic parameters are computed with ab initio electronic structure methods, is presented. Virtual photoluminescence experiments are performed on a prototypical PhOLED emission material consisting of 4,4′,4″-tris (N-carbazolyl)triphenylamine and fac-tris (2-phenylpyridine)iridium. The obtained TTA quenching rate is comparable to experimental results in the low-intensity limit.

Multiscale Simulation of Photoluminescence Quenching in Phosphorescent OLED Materials

Franz Symalla, Shahriar Heidrich, Pascal Friederich, Timo Strunk, Tobias Neumann, Daiki Minami, Daun Jeong, and Wolfgang Wenzel*

Bimolecular exciton-quenching processes such as triplet–triplet annihilation (TTA) and triplet–polaron quenching play a central role in phosphorescent organic light-emitting diode (PhOLED) device performance and are, therefore, an essential component in computational models. However, the experiments necessary to determine microscopic parameters underlying such processes are complex and the interpretation of their results is not straightforward. Here, a multiscale simulation protocol to treat TTA is presented, in which microscopic parameters are computed with ab initio electronic structure methods. With this protocol, virtual photoluminescence experiments are performed on a prototypical PhOLED emission material consisting of 93 wt% of 4,4′,4″-tris(*N*-carbazolyl)triphenylamine and 7 wt% of the green phosphorescent dye fac-tris(2-phenylpyridine)iridium. A phenomenological TTA quenching rate of 8.5×10^{-12} cm^3 s^{-1}, independent of illumination intensity, is obtained. This value is comparable to experimental results in the low-intensity limit but differs from experimental rates at higher intensities. This discrepancy is attributed to the difficulties in accounting for fast bimolecular quenching during exciton generation in the interpretation of experimental data. This protocol may aid in the experimental determination of TTA rates, as well as provide an order-of-magnitude estimate for device models containing materials for which no experimental data are available.

Dr. F. Symalla, Dr. T. Strunk, Dr. T. Neumann
Nanomatch GmbH
Hermann-von-Helmholtz-Platz 1
Bau 640, 76344 Eggenstein-Leopoldshafen, Germany
S. Heidrich, Dr. P. Friederich, Prof. W. Wenzel
Institute of Nanotechnology (INT)
Karlsruhe Institute of Technology (KIT)
Hermann-von-Helmholtz-Platz 1, 76344 Eggenstein-Leopoldshafen
Germany
E-mail: wolfgang.wenzel@kit.edu
Dr. D. Minami, Dr. D. Jeong
Samsung Advanced Institute of Technology
Samsung Electronics Co. Ltd.
130 Samsung-ro, Yeongtong-gu, Suwon-si, Gyeonggi-do 16678
Republic of Korea

1. Introduction

Low-cost organic materials with technological relevance are key constituents of a wide range of devices such as organic light emitting diodes (OLEDs),[1] organic photovoltaics,[2] and organic field effect transistors.[3] In the past few years, many investigations resulted in increasing device efficiency,[4] improvements of the manufacturing methods, the development of flexible devices, etc.[5] There is nearly an infinite variety of different organic materials—both small molecules and polymers—which can be used pure or in different mixtures and/or as multilayer structures.[6] Therefore, optimization in the form of experimental fabrication, small-scale production, and characterization of samples for material screening remains a costly challenge to experimentalists. Predictive analytical and computational modeling of candidate materials[7] may greatly reduce cost and accelerate the design of new materials. Bottom-up modeling further elucidates the physical processes in the device and may consequently offer great help in systematic material design. While recent work has seen progress regarding carrier mobility,[8] the ab initio treatment of excitonic processes, which play a key role in organic optoelectronic devices, remains an open challenge.[9]

The attainable internal quantum efficiency (IQE) in, for example, organic light-emitting diodes, organic photovoltaic devices, and light-emitting field-effect transistors is determined by the complex interplay of exciton radiative and nonradiative decay, diffusion, and dissociation. At high excitation densities, additional quenching can occur due to exciton–exciton and exciton–charge interactions. These bimolecular processes limit the IQE in phosphorescent OLEDs, in particular for high current density.[10] To further optimize devices, it is important to understand the origin of the effects behind roll-off and to disentangle the relative importance of different types of loss processes, also with respect to their impact on degradation.[11] Theoretical models on entire devices[12] must presently rely on estimates for the microscopic rates that have not been measured for the specific materials. In addition, triplet–triplet annihilation (TTA) processes are of paramount importance in fluorescent layers, where TTA leads to fluorescence efficiencies exceeding the spin-statistical limit.[13]

Experimental investigations[10,14] of quenching effects are limited by the availability of methods that enable the investigation of optoelectronic devices in-operando on a molecular level. For this reason, there is presently no full understanding of the relevant loss processes as a function of device architecture.[15] To fully understand roll-off, the nonuniform distribution of charge carriers and excitons and their interactions throughout the entire device, in particular in the emissive layers, need to be taken into account.

In order to better understand and control the complex loss processes, it is important to derive the relevant rates independently. A recent kinetic Monte Carlo (KMC) study of the roll-off in multilayer white OLEDs has revealed a fair agreement with experiment when using fitted triplet-polaron quenching and TTA Förster radii describing the quenching of excitons on fac-tris(2-phenylpyridine)iridium (Ir(ppy)$_3$) and bis(2-methyldibenzo [f,h]quinoxaline)(acetylacetonate)-iridium(III) of 3.0 nm.[12] In this work, we present a computational methodology to treat TTA as an important excitonic loss process with ab initio electronic structure methods. We then perform virtual photoluminescence-quenching experiments in digital twins of prototypical OLED emitting materials using KMC simulations in direct comparison to experiment.

TTA for phosphorescent OLEDs was for the first time reported by Baldo et al.[10a] based on the concept developed for anthracene crystals.[16] Triplet excitations can decay radiatively or transfer their energy to different molecules, which may or may not host another triplet excitation. Triplet energy transfer of an excited molecule ^3M to molecules in the ground state (e.g., as a Förster transfer) leads to exciton transport between molecules, while triplet energy transfer to another excited molecule $^3M'$ leads to TTA, which can be expressed formally[17] as a reaction

$$^3M + {}^3M' \rightarrow {}^0M + {}^3M'^* \rightarrow {}^0M + {}^3M' \tag{1.1}$$
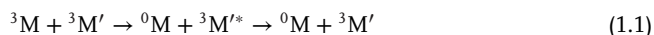
in which the highly excited triplet $^3M'^*$ typically decays nonradiatively into a low-lying triplet, losing most or all of its excess energy. In addition to the reduction in quantum efficiency, the dissipation of energy in this process may lead to degradation.

Time-resolved photoluminescence-quenching measurements have been used to investigate triplet transfer and annihilation.[17] In the experiments, a guest–host sample containing phosphorescent dyes is optically excited using a short laser pulse that generates a uniform triplet density $[n_{ex}](t = 0)$. After the excitation period, the time-dependent luminescence $L(t)$ of the sample is measured.

Considering only unimolecular triplet decay and TTA processes, the triplet density $[n_{ex}]$ evolves as

$$\frac{d[n_{ex}]}{dt} = -\frac{[n_{ex}]}{\tau} - \frac{1}{2}k_{TT}[n_{ex}]^2 \tag{1.2}$$

Here, k_{TT} is the reaction constant for the process in Equation (1.1) and $\tau = (\tau_{rad}^{-1} + \tau_{nonrad}^{-1})^{-1}$ is the exciton lifetime considering only monomolecular decay processes, which may be further separated into radiative (τ_{rad}) and nonradiative (τ_{nonrad}) decay. In case of the studied complexes, the intrinsic phosphorescent quantum yield is nearly 100%, so we approximate $\tau = \tau_{rad}$. Assuming that

Table 1. Parameters extracted from experimental photoluminescence measurements.[17]

	$[n_{ex}]$ [cm^{-3}]	k_{TT} [10^{-12} cm^3 s^{-1}]	τ [µs]
Experiment	$(9 \pm 5) \times 10^{18}$	0.8 ± 0.4	1.6 ± 0.05
	$(4 \pm 2) \times 10^{18}$	1.0 ± 0.6	1.6 ± 0.05
	$(7 \pm 5) \times 10^{17}$	2 ± 1	1.58 ± 0.05
	$(3 \pm 2) \times 10^{17}$	3 ± 2	1.58 ± 0.05
	$(9 \pm 5) \times 10^{16}$	7 ± 4	1.56 ± 0.05
	Mean	3 ± 2	1.58 ± 0.05

$L(t)$ is proportional to the exciton density $[n_{ex}](t)$, Equation (1.2) can be solved by

$$L(t) = \frac{L(0)}{(1 + [n_{ex}](0)k_{TT}\tau/2)e^{-t/\tau} - [n_{ex}](0)k_{TT}\tau/2} \tag{1.3}$$

When Equation (1.3) is fitted to the measured luminescence curves for different optical excitation intensities (and therefore different initial exciton densities $[n_{ex}](0)$), the TTA rate k_{TT} and the phosphorescence lifetime τ can be extracted. $[n_{ex}](0)$ is not directly accessible in experiment, because intensity-dependent decay processes occur before the measurement is actually started. As only the product of $[n_{ex}](0)$ and k_{TT} enters the equation separated in Equation (1.3), the accuracy of the experimental TTA analysis is limited in practice by the accuracy of the estimate of $[n_{ex}](0)$. This is reflected in the experimental results (see **Table 1**), where values extracted for k_{TT} at different illumination intensity varied over one order of magnitude for the same material. Since k_{TT} is a material-specific constant, this variation indicates that the lack of direct experimental access to $[n_{ex}](0)$ limits accuracy of the determination of TTA rates. These problems are absent in theoretical approaches, where the triplet density can be initialized instantaneously, but the accuracy of theoretical methods to compute the rates must be validated. Here, we validate such a methodology for the analysis of exciton quenching: using a KMC simulation of exciton dynamics, where the exciton density $[n_{ex}](t)$ is directly accessible at all times, we perform virtual photoluminescence experiments on a digital twin of a guest–host material comprising the phosphorescent dye Ir(ppy)$_3$ in a matrix of host molecules of 4,4′,4″-tris(N-carbazolyl)triphenylamine (TCTA) starting from first principles.

2. Experimental Section

Using rates computed from electronic structure calculations, we performed KMC simulations to compute time-resolved exciton trajectories and time-dependent photoluminescence. In the KMC simulations,[7b,18] we consider the processes/transitions illustrated in the top panel of **Figure 1**: 1) The excitation of molecules by absorption of light, that is, the creation of Frenkel excitons; 2) intersystem crossing; 3) energy transfer from an excited molecule to an unexcited molecule; 4) energy transfer from an excited molecule to another excited molecule, followed by a fast, thermal decay of the highly excited molecule to its original excitation state; and 5) radiative decay of excitons. KMC simulations assume that
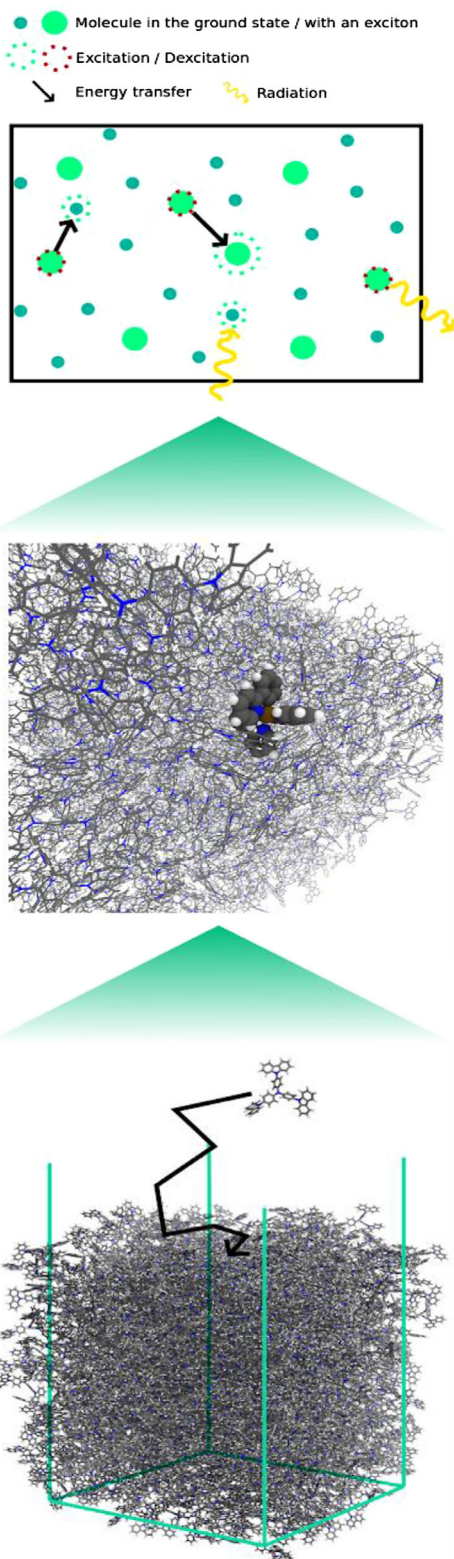
Figure 1. Multiscale simulation workflow from top down. Exciton dynamics are simulated in KMC. Excitons can be created, moved, decayed radiatively, and can undergo bimolecular quenching. Rates for these processes are computed from first principles on atomistic molecular morphologies. Morphologies are generated emulating physical vapor deposition.

the exciton dynamics are a chain of independent discrete events, for example, an exciton hopping from one molecule to the next, bimolecular quenching, radiative decay of an exciton, etc. A presupposition for this model is that all excitons are strongly localized on individual dye or host molecules. We describe the state of the system at any time by the excitation state of all molecules in the sample. A change of the system state then corresponds to change of the excitation state of the molecules that participate in a single specific process. In order to model the time dependence of the luminescence, we thus need to calculate the rates for all relevant transitions. The propagation of the system is then modeled as a succession of transitions of the system state, where different possible transitions can be understood as decay channels to each of which a rate is assigned.[19]

2.1. Models for the Rate Equations

In order to model the processes in the virtual experiment, we assume homogeneous photon absorption in a thin sample, that is, exciton generation rates are proportional to the oscillator strength of the individual molecules. The number of incident photons per area and time is given by $P/h\nu$, where P is the absorbed power, ν the frequency of the incident photon, and h is the Planck constant. In the high temperature limit, the radiative decay rate of the lowest triplet excitation is given by

$$\frac{1}{\tau} = \frac{1}{3} \sum_{\alpha=1}^{3} \frac{1}{\tau_\alpha} \tag{1.4}$$

where τ_α are the lifetimes of the three sublevels

$$\frac{1}{\tau_\alpha} = \frac{4}{3t_0} \alpha^3 E_{T_1\alpha}^3 |M_\alpha|^2 \tag{1.5}$$

where α is the fine structure constant, $E_{T_1\alpha}$ is the T_1 excitation energy, and M_α the dipole transition moment of the excitation. The dipole transition requires a spin flip and the moment is given by

$$\vec{M}_\alpha^A = \sum_{m=0} \frac{\left\langle \Psi_{S_m}^A \left| H_{S_0} \right| \Psi_{T_1\alpha}^A \right\rangle}{E_{T_1} - E_{S_m}} \times \left\langle \Psi_{S_0}^A |\vec{r}| \Psi_{S_m}^A \right\rangle$$

$$+ \sum_{m=1} \frac{\left\langle \Psi_{S_0}^A \left| H_{S_0} \right| \Psi_{T_m}^A \right\rangle}{E_{T_m} - E_{S_0}} \times \left\langle \Psi_{T_m}^A |\vec{r}| \Psi_{T_1\alpha}^A \right\rangle \tag{1.6}$$

where H_{S_0} is the spin–orbit Hamiltonian, S_m are the singlet excitations, and T_m the are triplet excitations. For a singlet transition, only one sublevel exists, and the transition dipole is given by

$$\vec{d}^A = \left\langle \Psi_{S_0}^A |\vec{r}| \Psi_{S_1}^A \right\rangle \tag{1.7}$$

We compute intermolecular energy transfer rates using the Born–Oppenheimer approximation and Fermi's golden rule

$$\omega_{if} = \frac{2\pi}{\hbar} \sum_h \sum_k p_h \left\langle \Psi_{fk} |H| \Psi_{ih} \right\rangle^2 \delta\left(E_{fk} - E_{ih}\right) \tag{1.8}$$

1900222 (3 of 10)

**ADVANCED
SCIENCE NEWS**

www.advancedsciencenews.com

**ADVANCED
THEORY AND
SIMULATIONS**

www.advtheorysimul.com

where i and f denote the initial and final electronic states, respectively, and h and k denote the initial and final vibrational states, respectively. $\Psi_{ih} = \Psi_i \Theta_h$ are then initial states and $\Psi_{fk} = \Psi_f \Theta_k$ are the final states, p_h are the occupational probabilities of the initial vibrational states. If we integrate the resonance condition over the vibrational states, the rate for the electronic transition from i to f is given by

$$\omega_{if} = \frac{2\pi}{\hbar} \left| J_{if} \right|^2 I \tag{1.9}$$

where $J_{if} = \langle \Psi_f | H | \Psi_i \rangle$ is the electronic coupling and I is the resonance integral.

The electronic coupling for an energy transfer from an initial state i to a final state f can be approximated by[20]

$$J_{if} = J_{if}^{\text{Foerster}} + J_{if}^{\text{Dexter}} + \frac{1}{2} \sum_j J_{ij}^{\text{CT}} J_{lf}^{\text{CT}} \left[\frac{1}{E_j^{\text{CT}} - E_i} + \frac{1}{E_j^{\text{CT}} - E_f} \right] \tag{1.10}$$

where j is a virtual charge–transfer (CT) state. The third term reflects a sequential hop of electron and hole, in which the intermediate state is virtual. J_{ij}^{CT} is the coupling between initial state i and CT state j. The Dexter term reflects a simultaneous CT of electron and hole and the Förster term reflects a coupling of excitation on molecule B coupled to a de-excitation on molecule A by a virtual photon. The Förster coupling is to first order given by[21]

$$J_{\text{AB}}^{\text{Foerster}} \approx \kappa^{\text{AB}} \frac{\left| \vec{d}^A \right| \cdot \left| \vec{d}^B \right|}{\left| R_{\text{AB}} \right|^3} \tag{1.11}$$

Here, $\vec{d}^X$ is the dipole transition moment of the respective excitation on molecule X, $\kappa = \hat{d}_A \cdot \hat{d}_B - 3(\hat{R}_{AB} \cdot \hat{d}_A)(\hat{R}_{AB} \cdot \hat{d}_B)$ an orientation factor, and $\hat{R}_{AB}$ is the center of geometry distance of the molecules A and B. For a triplet transition from S_0 to T_1, the transition moment $\vec{d}^X = \vec{M}_\alpha^X$ is given by Equation (1.6), where α is one of the three T_1 states. For a singlet, it is given by Equation (1.7). We approximate the Dexter coupling by

$$J_{if}^{\text{Dexter}} \approx$$

$$\sum_{n,m} \langle \Psi_A^{\text{HOMO}} | n \rangle \langle \Psi_B^{\text{HOMO}} | n \rangle \langle n | H | m \rangle \langle m | \Psi_A^{\text{LUMO}} \rangle \langle m | \Psi_B^{\text{LUMO}} \rangle \tag{1.12}$$

where $| \Psi_X^{\overset{\text{HOMO}}{\text{LUMO}}} \rangle$ are the highest occupied and the lowest unoccupied molecular orbitals on molecule X, and $|n\rangle$ and $|m\rangle$ indicate a complete basis. The approximation for the transfer integrals only holds if the HOMO–LUMO transition is the main contribution to the excitation.

The summation over the phonon modes, namely the computation of the resonance integral J_{if} in Equation (1.9), leads to two widely used frameworks to compute the microscopic rates: Marcus theory[22] holds in the high-temperature limit and assumes a classical vibrational excitation to a transition state of the

charge/energy transfer. For the opposite case, that is, when the energy quanta of the vibrational modes are significantly larger than the effective temperature, the (also classical) resonance condition of Miller–Abrahams rates[23] is more suitable. De Vries et al.[24] showed that a fully quantum mechanical transition rate that takes vibrational resonance into account explicitly yields a rate between Marcus and Miller–Abrahams rates depending on the force constants of the relevant vibrations involved.

For excitations with hard reaction coordinates, few vibrations can absorb excess energy without a severe distortion of the geometry, that is, a reduction of the Franck–Condon factor. This resonance behavior is well-represented by Miller–Abraham rates where the resonance condition is set to unity for all final states with energy lower than the initial state. As for TTA, we have many possible acceptor states T_n, it stands to reason that some of them would involve structural reorganization along a hard reaction coordinate, that is, allowing for excess energy absorption, so that we deem Miller–Abrahams rates a reasonable approximation for TTA. In the Miller–Abrahams limit, Equation (1.9) becomes

$$\omega_{if} = \nu_0 \frac{2\pi}{\hbar} \left| J_{if}^2 \right| \min \left(1, \exp \left(-\frac{\Delta E_{if}}{k_B T} \right) \right) \tag{1.13}$$

where $\nu_0 \frac{2\pi}{\hbar}$ is an attempt frequency. This rate stays in resonance as long as the final state is lower in energy than the initial state. For a bimolecular energy transfer, this would correspond to a reaction coordinate associated with a high vibrational frequency.

The lowest excited triplet cannot recombine radiatively without a spin flip (see Equations (1.5) and (1.6)), which leads to lifetimes > 1 μs for typical phosphorescent organic dyes. The long lifetime results in an increased probability for an energy transfer from one triplet to another with a rate for TTA processes given by

$$\omega_{\text{TTA}}^{\text{AB}} =$$

$$\nu_0 \frac{2\pi}{\hbar} \sum_{n=1} \left| J_n^{\text{AB}} \right|^2 \min \left(1, \exp \left(-\frac{\left[E_{T_n}^B - E_{T_1}^B \right] - \left[E_{S_0}^A - E_{T_1}^A \right]}{k_B T} \right) \right) \tag{1.14}$$

where we set $\nu_0 = 1/\sqrt{4\pi \lambda_n^{\text{AB}} k_B T}$. The sum is over possible acceptor states to which the triplet on molecule B can be excited. The Förster part of the electronic coupling is given by

$$J_n^{\text{AB}} \approx \sum_{\alpha=1}^3 \kappa_\alpha^{\text{AB}} \frac{\left| \vec{M}_\alpha^A \right| \cdot \left| \langle \Psi_{T_1}^B | \vec{r} | \Psi_{T_n}^B \rangle \right|}{\left| R_{\text{AB}} \right|^3} \tag{1.15}$$

where $\vec{M}_\alpha^A$ are the dipole transition moments for phosphorescence on A and $\langle \Psi_{T_1}^B | \vec{r} | \Psi_{T_n}^B \rangle$ transition dipoles for transitions from T_1 to T_n on molecule B.

1900222 (4 of 10)

**ADVANCED
SCIENCE NEWS**

www.advancedsciencenews.com

**ADVANCED
THEORY AND
SIMULATIONS**

www.advtheorysimul.com

2.2. Simulation Protocol

Using these rate equations, we performed virtual TTA experiments on off-lattice morphologies comprising $\mathcal{O}(10^6)$ molecules, where each molecule is represented by its center of geometry position and its excitation state. Presently, quantum calculations in the matrix are too costly to compute all energies and rates for systems of this size. We, therefore, performed these calculations on smaller samples, henceforth called atomistic morphologies, from which we derived the distribution functions of relevant observables, such as energies and rates. Based on this data set, we generate fictitious extended morphologies following a stochastic procedure.[7b] The molecular positions for the extended morphology are generated using an iterative Boltzmann inversion, reproducing the center-of-geometry radial distribution function of atomistic morphologies. The radial distribution functions were extracted from atomistic (93:7) morphologies of $\mathcal{O}(10^3)$ molecules. Herein and in the following, (X:Y) denotes the ratio of host to guest molecules in the mixture. This morphology was generated with Deposit, a molecular modeling approach mimicking physical vapor deposition.[25] Using this approach, one molecule is added to an initially empty simulation box one at a time and equilibrated into a thermodynamically relaxed state using 30 Monte Carlo based basin-hopping cycles consisting of 150k simulation steps each, annealing from 4000 to 300 K. The bottom layers are discarded to avoid edge effects; the simulation box is periodic in the XY direction. The interaction between a newly added molecule and already deposited molecules is computed at each simulation step using customized forcefields comprising Lennard–Jones and Coulomb-potential using partial charges from the ESP fit.[26] Intramolecular interactions for rotations around flexible dihedral angles are computed using a spline-potential fitted to energies from density functional theory (DFT) calculations for the individual molecules.

The distribution of molecular excitation energies and intermolecular electronic couplings are calculated on the atomistic morphologies using the Quantum Patch method,[27] a density embedding method that incorporates polarization effects from the environment on molecular properties. T_1 energies of a set of 25 different $Ir(ppy)_3$ molecules in the (89:11) system were also computed with this method to fit a Gaussian distribution of energy values. According to this distribution, we then assigned a T_1 energy to each molecule in the expanded system. To obtain S_1 energies, we added to each T_1 energy the S_1-T_1 gap as obtained in vacuum calculations using TDDFT with the B3LYP functional and the def2-SVP basis set as implemented in TURBOMOLE[28] for each individual site. CT and Dexter transfer integrals for exciton energy-transfer were computed based on Equations (1.10) and (1.12) using the innermost 515 molecules of the atomistic (89:11) morphology. We mapped the transfer integrals on all pairs of the extended morphology using the procedure outlined in Symalla et al.[18c] Using Equation (1.13), we calculated CT and Dexter energy transfer rates for all pairs in the system. Rates for singlet–singlet Förster energy transfer between two molecules (S_1-S_1) were obtained by calculating transition dipoles of the singlet excitation (S_0 to S_1) of TCTA and $Ir(ppy)_3$ in vacuum using TDDFT with the B3LYP exchange-correlation functional and the def2-SVP basis functions as implemented in the TURBOMOLE package.[28] The transition dipoles were then mapped onto the

point distribution of the extended morphology by randomly assigning a direction to the vacuum transition dipoles.

Using Equations (1.11) and (1.13), distance-dependent distributions of rates $\omega(r)$ for the singlet Förster energy transfers were calculated and mapped onto a stochastic model for a numerically efficient rate evaluation during the KMC simulations. Förster rates for triplet transport (energy transfer from triplet to neutral molecule in the ground state, T_1-T_1) as well as TTA between $Ir(ppy)_3$ molecules were obtained by calculating the phosphorescent transition dipole moments of $Ir(ppy)_3$ in vacuum using the method of Jansson et al.[29] as implemented in the DALTON package. As TTA acceptor states, we computed the first 45 excitations of $Ir(ppy)_3$ from the T_1 state using TDDFT with B3LYP and the def2-SVP basis set with TURBOMOLE. Similar to the procedure applied to generate the singlet energy distribution, the phosphorescent transition dipole moments were then mapped onto the extended morphology by randomly rotating the set of vacuum moments. Using Equations (1.11), (1.14), and (1.15), Förster rates for the T_1-T_1 energy transfers as well TTA energy transfer were calculated and mapped on a distance-dependent distribution of rates $\omega(r)$ for evaluation during KMC simulations.

The rates for all processes on the extended morphology were computed as described above, and photoluminescence quenching was simulated with off-lattice KMC using the LightForge package. For the first $t_c = 2.5 \times 10^{-8}$ s of each simulation, excitons were generated on random sites of the off-lattice morphology with different illumination intensities under the assumption that every photon is absorbed, resulting in an initial exciton density at t_c corresponding to $[n_{ex}](0)$ at the start of the photoluminescence-quenching measurement. At each KMC simulation step, a single process (creation of a singlet, intersystem crossing, move of a single exciton to a neighboring site via Förster, Dexter or CT, energy transfer between two excitons [TTA], or radiative decay of a specific exciton) was drawn from a list of all possible processes according to their specific rates, and a time-step computed based on the total decay rate of the system, before picking the next move. The number of photon emissions (radiative decays) over time was extracted to analyze photoluminescence quenching.

3. Results and Discussion

In the following, we model photoluminescence quenching in comparison to photoluminescence measurements in a prototypical OLED emission material consisting of 93 wt% of TCTA and 7 wt% of the green phosphorescent dye $Ir(ppy)_3$.[17] Microscopic rates for TTA and exciton transport were computed from first principles, based on an atomistic morphology generated with Deposit, as described in the Experimental Section. We found that the T_1 energies for $Ir(ppy)_3$ follow a Gaussian distribution with a mean of 2.0 eV and a standard deviation of 0.044 eV. The quality of these phosphorescence transition moments can be evaluated by calculating the radiative lifetime of $Ir(ppy)_3$ according to Equation (1.4). Using the S_0 geometry of $Ir(ppy)_3$, we obtain a radiative lifetime of 1.4 μs, close to the experimental values between 1 and 2 μs.[30] We would like to note that although good agreement between experimental and calculated radiative lifetimes is obtained if we calculate the T_1-S_0 transition moment at

**ADVANCED
SCIENCE NEWS**
www.advancedsciencenews.com

**ADVANCED
THEORY AND
SIMULATIONS**
www.advtheorysimul.com
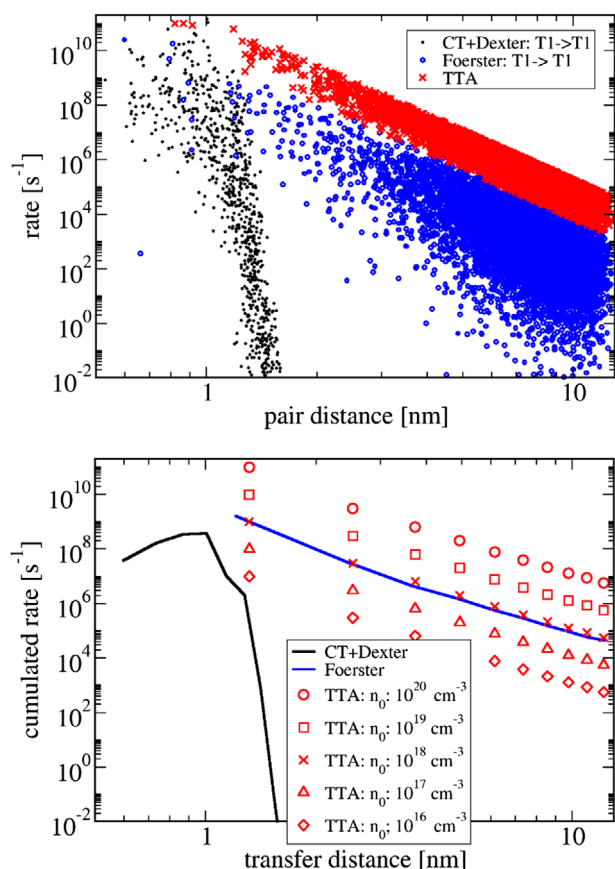
Figure 2. Top: Distance dependence of triplet transition rates between pairs of Ir(ppy)$_3$ molecules as a function of distance. For short distances, triplet transport via Förster (blue circles) and via CT or Dexter (black dots) processes are of similar order of magnitude. For longer distances triplet transport is only possible due to Förster energy transfer. The pair rates for TTA (red crosses) are two orders of magnitude larger than for T$_1$-T$_1$ energy transfer. Bottom: Cumulated triplet transfer rates to all acceptors (emitters for T$_1$-T$_1$ transport, excitons for TTA) in a given distance, via CT or Dexter (black line) and Förster (blue line) processes. Red symbols show the TTA rates for different exciton concentrations. Emitter concentration is 8%. Except for very high exciton concentrations, Förster transfer to another emitter is more likely than TTA.

the S$_0$ geometry as done in this work, lifetimes obtained using relaxed molecular geometries of the T$_1$ state are smaller by a factor of 5–6. Jansson et al. argue that phosphorescent properties should be intermediate between results calculated at the S$_0$ and T$_1$ geometries,[29] which means that the employed quadratic response method might underestimate transition moments if the calculation were performed on a more representative transition geometry. Self-consistent spin–orbit coupling methods might offer a more accurate alternative to predictively calculate radiative decay rates.

The distribution of molecular excitation energies and intermolecular electronic couplings were calculated as described in the Experimental Section. The distributions of the resulting bimolecular rates for TTA and Förster triplet transport (Förster T$_1$-T$_1$) as well as triplet transport by Dexter/CT (Dexter/CT T$_1$-T$_1$) between Ir(ppy)$_3$ molecules are shown in **Figure 2**. For neighboring molecules, CT/Dexter-based (which require wave function over-

lap) and Förster-based energy transfer rates are distributed over similar orders of magnitude (10^8–10^9 s^{-1}). For larger pair distances, the rates for overlap based energy transfer drop while the envelope of the rate distribution for Förster mediated transfer is proportional to R^{-6}. The envelope of the rates for TTA processes is two orders of magnitude higher than that for the Förster triplet transfer to a neutral molecule (T$_1$-T$_1$). We find that the distribution for the TTA rates is orders of magnitude narrower than for the T$_1$-T$_1$ transfer. The reason for the large spread in the T$_1$-T$_1$ rates is different mutual orientations of the transition moments involved. As we sum over many target states for the TTA rates, by contrast, orientation disorder averages out more strongly, resulting in a smaller spread.

The total rate for an energy transfer over a distance r depends on the number of target states and is given by the sum of all rates to potential acceptor molecules in the interval $r, r + dr$. For TTA, the number of target states, therefore, depends on the exciton concentration. Total rates for TTA and energy transfers are shown in Figure 2, bottom panel. We can see that although bimolecular TTA rates are higher than transport rates, the total TTA rate at realistic exciton concentrations is lower than transport rates, indicating that exciton diffusion is likely to occur prior to TTA.

The mean distance dependence of bimolecular rates for the dominant energy transfer processes between the different combinations of TCTA and Ir(ppy)$_3$ is shown in **Figure 3**. Rates for singlet transport from TCTA to either TCTA or Ir(ppy)$_3$ are dominated by Förster energy transport and are of the order of 10^{11} s^{-1} for short distances. Triplets can only move from the host TCTA via CT-induced transfer to the unoccupied guest Ir(ppy)$_3$ or to TCTA molecules with rates of the order of 10^9 s^{-1}/10^8 s^{-1}, respectively. Exciton transport rates from Ir(ppy)$_3$ to TCTA are negligible, as T$_1$ energies on Ir(ppy)$_3$ are 0.5 eV below the T$_1$ energies of TCTA.

In order to compare the bimolecular TTA rates determined in this work to systems analyzed in different studies,[23] we fitted the bimolecular TTA and triplet transport rates to the phenomenological equation $\omega(R) = \frac{1}{\tau_{rad}} \frac{R_0}{R}$ and determined bimolecular Förster radii for TTA and triplet diffusion in Ir(ppy)$_3$. With a radiative triplet lifetime of 1.6 μs, we determine a Förster radius of 6.5 nm for TTA and 2.5 nm for the triplet diffusion. We would like to emphasize that in a solid, exciton diffusion also depends on the density of acceptor molecules, so that there is no direct relationship between diffusion length and the bimolecular Förster radius.

Based on the calculated rates, we performed photoluminescence simulations using the LightForge kinetic Monte Carlo code[18b,c,31] on extended off-lattice morphologies comprising $\mathcal{O}(10^6)$ molecules. The simulations were initialized with illumination times of 2.5×10^{-8} s and varying illumination intensities from 6 to 50 W cm^{-2}, leading to exciton concentrations from 2.1×10^{-17} to 1.7×10^{18} cm^{-3} (see **Table 2**) at the time exciton generation was stopped. The rates for TTA and the transport processes were assigned randomly according to the distributions calculated above (see Figures 2 and 3). We used a radiative triplet lifetime on Ir(ppy)$_3$ of 1.6 μs and assumed that intersystem crossing on Ir(ppy)$_3$ is quasi-instantaneous (10^{14} s^{-1}), that is, all singlets on Ir(ppy)$_3$ are converted to triplets. Thermal decay was assumed to be negligible compared to transport and radiative decay rates.

ADVANCED
SCIENCE NEWS
www.advancedsciencenews.com

ADVANCED
THEORY AND
SIMULATIONS
www.advtheorysimul.com
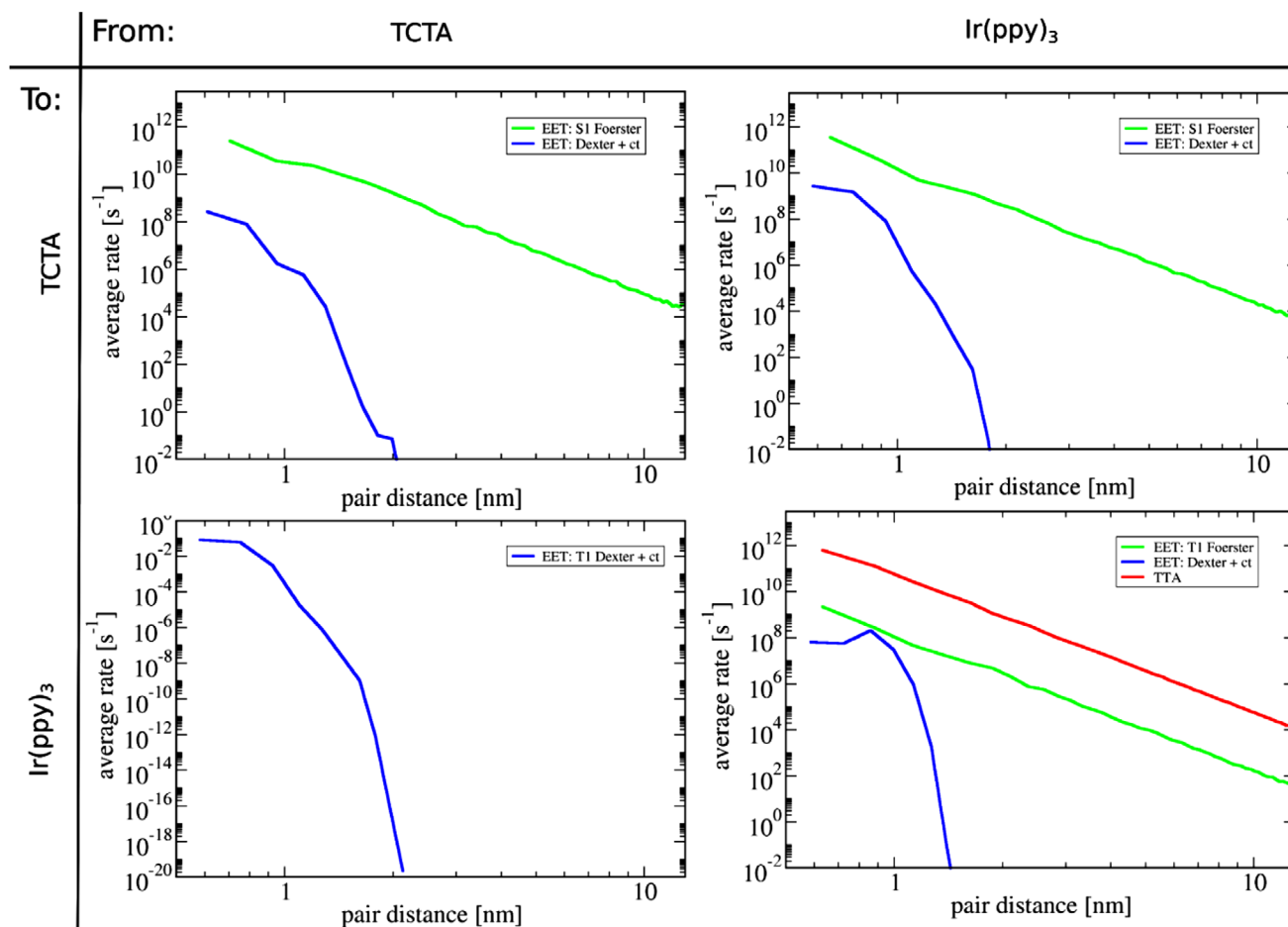
Figure 3. Dominant exciton energy transport rates of respective molecule combinations in TCTA:Ir(ppy)$_3$. Average rates for different energy transfers between two molecules are plotted. Energy transport on TCTA is dominated by Förster energy transfer for singlets. For triplets, only Dexter and CT type of energy transfer is possible. Rates from TCTA to Ir(ppy)$_3$ are increased as the optical gap on Ir(ppy)$_3$ is smaller than on TCTA. For the same reason, a transfer back from Ir(ppy)$_3$ to TCTA is strongly suppressed (T$_1$-T$_1$ via Dexter is the leading but still unlikely process). Between Ir(ppy)$_3$ molecules, TTA has higher rates than a T$_1$-T$_1$ energy transfer.

Table 2. Parameters determined in the time-resolved photoluminescence simulations. The table shows average exciton densities after initial illumination for four different illumination intensities. Values for the TTA constant k_{TT} and lifetime τ are obtained by fitting the simulated luminescence to Equation (1.3).

	$[n_{ex}]$ [cm^{-3}]	k_{TT} [10^{-12} cm^3 s^{-1}]	τ [µs]
Simulation	1.7×10^{18}	8.5	1.7
	9.7×10^{17}	8.1	1.5
	3.1×10^{17}	8.6	1.5
	2.1×10^{17}	8.8	1.5
	Mean	8.5	1.5

After exciton generation is stopped, we measure the exciton density and start tracking the number of emitted photons over time in the KMC simulation. The simulation terminates when all excitons in the sample have decayed. For each initial illumination intensity, we repeated this measurement 45 times and calculated the average initial exciton density and time dependence of the luminescence. The results for three different initial exciton densities are shown in the lower panel of **Figure 4**. The upper panel shows experimental photoluminescence measurements by Reineke et al.[17] for the same system. The exponential decay in the tail of the plots corresponds to independent (mostly radiative) decay of the triplets, so that the exciton lifetime can be read off from the slope of the logarithm of the luminescence. The initial nonlinear part of the decay curve corresponds to an exciton annihilation mechanism depending on the exciton concentration, that is, TTA.

By fitting the logarithm of luminescence L to Equation (1.3), we obtain $L(0)$, k_{TT}, and τ. We would like to note that while the radiative lifetime is a simulation parameter, the lifetime extracted from the fit contains all effective independent decay mechanisms. The results for the TTA constant k_{TT} and the lifetime τ are shown in Table 2. For all exciton concentrations, the fit lifetimes are between 1.5 and 1.7 µs, virtually identical to the radiative lifetime of the triplets (1.6 µs).

The luminescence fits result in an average TTA constant k_{TT} of 8.5×10^{-12} cm^3 s^{-1}. k_{TT} changes little for all exciton densities considered. The simulation result for the average k_{TT} is astonishingly close to the experimental value of $7 \pm 4 \times 10^{-12}$ cm^3 s^{-1}

ADVANCED
SCIENCE NEWS

www.advancedsciencenews.com

ADVANCED
THEORY AND
SIMULATIONS

www.advtheorysimul.com
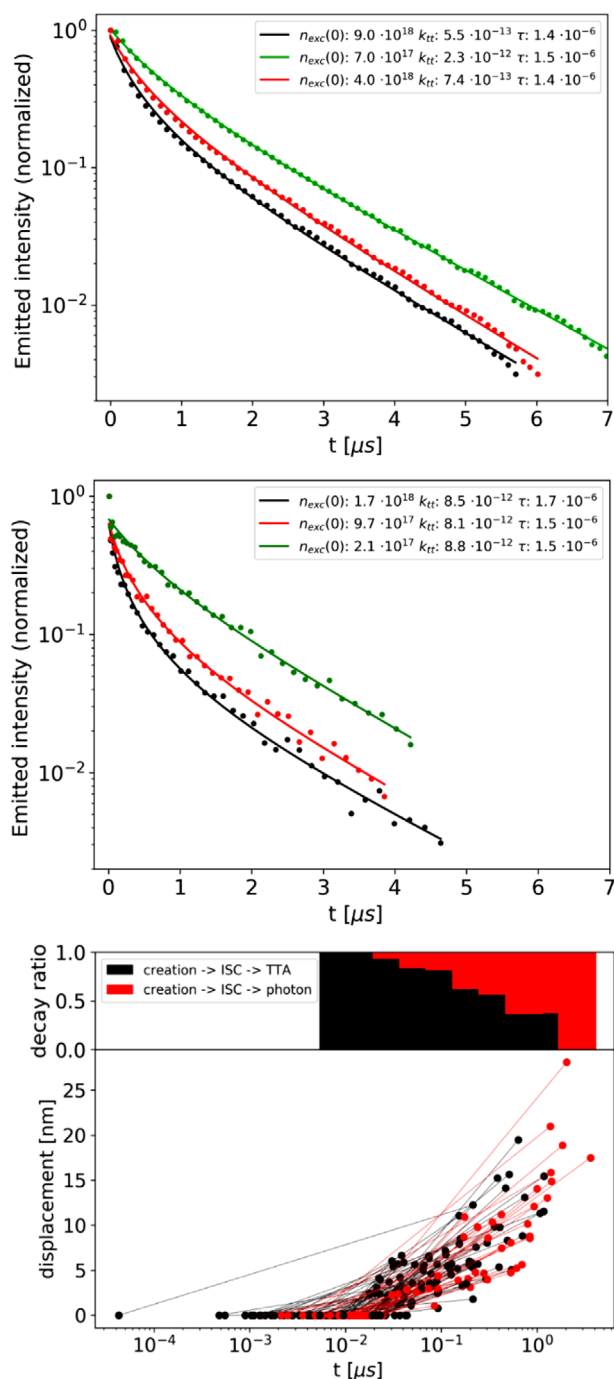
Figure 4. Photoluminescence intensity over time after creation of initial exciton density n_{ex} by illumination with a laser for TCTA:Ir(ppy)$_3$. The top panel shows experimental measurements[17] and the middle panel shows the results from the proposed multiscale model. Different initial exciton densities n_{ex} are shown by different colors. The linear tail of the time dependence of the light intensity corresponds to the independent decay of excitons with a lifetime τ. The nonlinear decay at early times is due to TTA. The higher the initial exciton density, the more pronounced the nonlinear part reflecting the TTA. Bottom panel: Life cycle of excitons: Lines connect time of creation with the time and displacement of annihilation of individual excitons. Excitons indicated in red decay radiatively, black by TTA. The upper panel shows the fractions of TTA and radiative decay over time, respectively.

at low illumination. The experimentally determined parameters of Reineke et al.[17] are shown in Table 1. In contrast to our simulations, the experimental k_{TT} increase with decreasing estimated exciton concentrations. Since this increase shows a systematic trend, we speculate that the reason for this could be an overestimation of the initial exciton densities at stronger illumination in experiment, due to a negligence of immediate TTA. Conversely, this would indicate that the errors in the density estimate are smaller for lower intensities.

The lifecycle of excitons during one photoluminescence-quenching simulation is shown in Figure 4. Early in the process, most excitons are destroyed via TTA due to the high exciton density. Later, the exciton diffusion length increases as exciton concentration decreases. At the end of the simulation, when exciton densities are low, radiative decay is the predominant decay mechanism and we can observe diffusion lengths of over 20 nm for individual excitons.

4. Conclusion

In summary, we analyzed TTA in an OLED emission layer comprising TCTA doped with the phosphorescent emitter Ir(ppy)$_3$. Using virtual photoluminescence-quenching experiments on a digital twin of the emission layer, we computed a value for the phenomenological TTA quenching rate k_{TT} from first principles and compared our results to experimental data. Based on this approach, we calculated bimolecular TTA and exciton transport rates for a mixed system of TCTA:Ir(ppy)$_3$. From the photoluminescence measurements in KMC simulations, we could extract a value for the phenomenological TTA quenching rate k_{TT} of 8.5×10^{-12} cm^3 s^{-1} that corresponds closely to experimental results at low illumination.[17] We note that k_{TT} is independent of the initial exciton density $[n_{ex}](0)$ in the simulations, whereas the experimentally determined value varies from 0.8×10^{-12} cm^3 s^{-1} at high initial exciton densities to 7.4×10^{-12} cm^3 s^{-1} at very low initial exciton densities. As mentioned in the introduction, the product of $[n_{ex}](0)$ and k_{TT} cannot be disentangled in the photoluminescence model applied to extract k_{TT} from (both virtual and real) experiment, and the dependence of experimentally determined k_{TT} can be traced back to a systematic inaccuracy in the determination of $[n_{ex}](0)$ in experiment. Comparison of computed and measured k_{TT} gives rise to the assumption that the model to estimate $[n_{ex}](0)$ in experiment holds only for weak illumination intensity $L(0)$, due to a negligence of very fast bimolecular quenching during the exciton generation in the estimation of the initial exciton density. These results validate the multiscale simulation approach developed in this investigation. Because the low illumination limit may be hard to reach in experiments, the methods developed in this article may aid to determine TTA rates experimentally or serve as an order-of-magnitude estimate for device models, where such rates are not available.

Mesta et al. have previously analyzed the roll-off in OLED devices based on heuristic KMC models.[12] They investigated various scenarios for the ratio between the exciton diffusion radius and the TTA radius and found that the experimental data could be fitted under the assumption that $R_{F;TTA} = 2R_{F;diff}$. This assumption is validated by our calculations, but our results differ in the absolute value of the Förster radius by roughly a factor

of two. However, as is shown in Figure 2, the relative importance of the diffusion and TTA processes depends on emitter density, site connectivity, and the exciton density. As exciton quenching in an OLED involves processes other than TTA and depends on the detailed charge carrier balance and width of the recombination zones, we cannot expect identical Förster radii to our simulations, because the parameters are extracted to optimize the overall fit to the data. In the photoluminescence-quenching experiments, high exciton concentrations are achieved by strong illumination. In the simulations by Mesta et al., IQEs are overestimated at high currents/exciton concentrations and larger Förster radii may ameliorate this discrepancy.

The KMC calculations serve as a computational microscope to investigate the competing processes as indicated in Figure 4. Variation of emitter density and layer thickness in devices enables optimization of roll-off. In the system investigated here, excitons have a high probability to diffuse before they decay by either TTA or photon emission. Suppressing the diffusion processes by lowering the emitter concentration will reduce roll-off by shortening the effective radius an exciton can travel to reach another exciton, which may then lead to reduced TTA. In this sense, the present model can be used as a tool for stack optimization.

On a final note, we would like to comment on the use of Miller–Abrahams theory to derive the rate equation for TTA. In a full quantum treatment of the exciton hopping rates,[24] excitations along reaction coordinates with stiff vibrational modes contribute strongly to the acceptance probability of the excitation energy from the donor, as they have a larger resonance window. According to TDDFT calculations, there are 15 acceptor excitations of T_1 with an energy around and below 2.0 eV, the energy of the decaying donor triplet on Ir(ppy)$_3$. If there is one dominant contribution to the sum in Equation (1.8), the rate as a whole will be approximated well by the Miller–Abrahams rate expression, but significantly underestimated if Marcus rates are used instead.

Conflict of Interest

The authors declare no conflict of interest.

[1] a) C. Groves, *Nat. Mater.* **2013**, *12*, 597; b) L. Hung, C. Chen, *Mater. Sci. Eng., R* **2002**, *39*, 143.

[2] a) A. W. Hains, Z. Liang, M. A. Woodhouse, B. A. Gregg, *Chem. Rev.* **2010**, *110*, 6689; b) B. Kippelen, J.-L. Brédas, *Energy Environ. Sci.* **2009**, *2*, 251; c) G. Li, R. Zhu, Y. Yang, *Nat. Photonics* **2012**, *6*, 153.

[3] C. D. Dimitrakopoulos, P. R. Malenfant, *Adv. Mater.* **2002**, *14*, 99.

[4] a) M. A. Green, K. Emery, Y. Hishikawa, W. Warta, E. D. Dunlop, *Prog. Photovoltaics* **2015**, *23*, 1; b) N. T. Kalyani, S. Dhoble, *Renewable Sustainable Energy Rev.* **2012**, *16*, 2696; c) I. G. Lezama, A. F. Morpurgo, *MRS Bull.* **2013**, *38*, 51; d) S. Shrestha, *Prog. Photovoltaics* **2013**, *21*, 1429.

[5] a) J. Hast, M. Tuomikoski, R. Suhonen, K. Väisänen, M. Välimäki, T. Maaninen, P. Apilo, A. Alastalo, A. Maanineny, *Dig. Tech. Pap. - Soc. Inf. Disp. Int. Symp.* **2013**, *44*, 192; b) C. N. Hoth, P. Schilinsky, S. A. Choulis, S. Balasubramanian, C. J. Brabec, in *Applications of Organic and Printed Electronics* (Ed: E. Cantatore), Springer, Berlin **2013**, pp. 27–56.

[6] R. Gómez-Bombarelli, J. Aguilera-Iparraguirre, T. D. Hirzel, D. Duvenaud, D. Maclaurin, M. A. Blood-Forsythe, H. S. Chae, M. Einzinger, D.-G. Ha, T. Wu, G. Markopoulos, S. Jeon, H. Kang, H. Miyazaki, M. Numata, S. Kim, W. Huang, S. I. Hong, M. Baldo, R. P. Adams, A. Aspuru-Guzik, *Nat. Mater.* **2016**, *15*, 1120.

[7] a) P. Friederich, A. Fediai, S. Kaiser, M. Konrad, N. Jung, W. Wenzel, *Adv. Mater.* **2019**, *31*, 1808256; b) P. Kordt, J. J. M. van der Holst, M. Al Helwi, W. Kowalsky, F. May, A. Badinski, C. Lennartz, D. Andrienko, *Adv. Funct. Mater.* **2015**, *25*, 1955.

[8] a) P. Friederich, V. Meded, A. Poschlad, T. Neumann, V. Rodin, V. Stehr, F. Symalla, D. Danilov, G. Lüdemann, R. F. Fink, I. Kondov, F. von Wrochem, W. Wenzel, *Adv. Funct. Mater.* **2016**, *26*, 5757; b) P. Friederich, V. Gómez, C. Sprau, V. Meded, T. Strunk, M. Jenne, A. Magri, F. Symalla, A. Colsmann, M. Ruben, W. Wenzel, *Adv. Mater.* **2017**, *29*, 1703505.

[9] D. Jacquemin, D. Escudero, *Chem. Sci.* **2017**, *8*, 7844.

[10] a) M. A. Baldo, C. Adachi, S. R. Forrest, *Phys Rev B* **2000**, *62*, 10967; b) C. Murawski, K. Leo, M. C. Gather, *Adv. Mater.* **2013**, *25*, 6801.

[11] a) H. van Eersel, P. A. Bobbert, R. A. J. Janssen, R. Coehoorn, *J. Appl. Phys.* **2016**, *119*, 163102; b) H. van Eersel, P. A. Bobbert, R. A. J. Janssen, R. Coehoorn, *Appl. Phys. Lett.* **2014**, *105*, 143303.

[12] M. Mesta, H. van Eersel, R. Coehoorn, P. A. Bobbert, *Appl. Phys. Lett.* **2016**, *108*, 133301.

[13] D. Y. Kondakov, T. D. Pawlik, T. K. Hatwar, J. P. Spindler, *J. Appl. Phys.* **2009**, *106*, 124510.

[14] a) N. C. Giebink, S. R. Forrest, *Phys. Rev. B* **2008**, *77*, 235215; b) S. Reineke, K. Walzer, K. Leo, *Phys. Rev. B* **2007**, *75*, 125328; c) D. Song, S. Zhao, Y. Luo, H. Aziz, *Appl. Phys. Lett.* **2010**, *97*, 243304; d) F. X. Zang, T. C. Sum, A. C. H. Huan, T. L. Li, W. L. Li, F. Zhu, *Appl. Phys. Lett.* **2008**, *93*, 023309.

[15] J. Lee, C. Jeong, T. Batagoda, C. Coburn, M. E. Thompson, S. R. Forrest, *Nat. Commun.* **2017**, *8*, 15566.

[16] R. Kepler, J. Caris, P. Avakian, E. Abramson, *Phys. Rev. Lett.* **1963**, *10*, 400.

[17] S. Reineke, K. Walzer, K. Leo, *Phys. Rev. B* **2007**, *75*, 125328.

[18] a) M. Mesta, M. Carvelli, R. J. de Vries, H. van Eersel, J. J. M. van der Holst, M. Schober, M. Furno, B. Lüssem, K. Leo, P. Loebl, R. Coehoorn, P. A. Bobbert, *Nat. Mater.* **2013**, *12*, 652; b) F. Symalla, P. Friederich, S. Kaiser, T. Strunk, T. Neumann, W. Wenzel, *Dig. Tech. Pap. - Soc. Inf. Disp. Int. Symp.* **2018**, *49*, 340; c) F. Symalla, P. Friederich, A. Massé, V. Meded, R. Coehoorn, P. Bobbert, W. Wenzel, *Phys. Rev. Lett.* **2016**, *117*, 276803.

[19] V. Rodin, F. Symalla, V. Meded, P. Friederich, D. Danilov, A. Poschlad, G. Nelles, F. von Wrochem, W. Wenzel, *Phys. Rev. B* **2015**, *91*, 155203.

**ADVANCED
SCIENCE NEWS**

www.advancedsciencenews.com

**ADVANCED
THEORY AND
SIMULATIONS**

www.advtheorysimul.com

[20] J. Wehner, B. Baumeier, *J. Chem. Theory Comput.* **2017**, *13*, 1584.

[21] B. Fückel, A. Köhn, M. E. Harding, G. Diezemann, G. Hinze, T. Basché, J. Gauss, *J. Chem. Phys.* **2008**, *128*, 074505.

[22] R. A. Marcus, *Rev. Mod. Phys.* **1993**, *65*, 599.

[23] A. Miller, E. Abrahams, *Phys. Rev.* **1960**, *120*, 745.

[24] X. de Vries, P. Friederich, W. Wenzel, R. Coehoorn, P. A. Bobbert, *Phys. Rev. B* **2018**, *97*, 075203.

[25] T. Neumann, D. Danilov, C. Lennartz, W. Wenzel, *J. Comput. Chem.* **2013**, *34*, 2716.

[26] U. C. Singh, P. A. Kollman, *J. Comput. Chem.* **1984**, *5*, 129.

[27] P. Friederich, F. Symalla, V. Meded, T. Neumann, W. Wenzel, *J. Chem. Theory Comput.* **2014**, *10*, 3720.

[28] R. Ahlrichs, M. Bär, M. Häser, H. Horn, C. Kölmel, *Chem. Phys. Lett.* **1989**, *162*, 165.

[29] E. Jansson, B. Minaev, S. Schrader, H. Ågren, *Chem. Phys.* **2007**, *333*, 157.

[30] a) W. J. Finkenzeller, H. Yersin, *Chem. Phys. Lett.* **2003**, *377*, 299; b) T. Hofbeck, H. Yersin, *Inorg. Chem.* **2010**, *49*, 9290.

[31] Nanomatch GmbH, LightForge KMC, http://www.nanomatch.com/lightforge-kmc/ (accessed: February 2020).